

Testing the Alfvén-wave model of the solar wind with interplanetary scintillation

MUNEHITO SHODA,¹ KAZUMASA IWAI,² AND DAIKOU SHIOTA^{2,3}

¹*National Astronomical Observatory of Japan, National Institutes of Natural Sciences, 2-21-1 Osawa, Mitaka, Tokyo, 181-8588, Japan*

²*Institute for Space-Earth Environmental Research, Nagoya University, Furo-cho, Chikusa-ku, Nagoya, 464-8601, Japan*

³*National Institute of Information and Communications Technology (NICT), Nukui-Kita-machi, Koganei, Tokyo, 184-8795 Japan*

ABSTRACT

Understanding the mechanism(s) of the solar wind acceleration is important in astrophysics and geophysics. A promising model of the solar wind acceleration is known as the wave/turbulence-driven (WTD) model, in which Alfvén waves feed energy to the solar wind. In this study, we tested the WTD model with global measurement of wind speed from interplanetary scintillation (IPS) observations. For Carrington rotations in minimal and maximal activity phases, we selected field lines calculated by the potential-field source-surface method in high- and mid-latitudes and compared the simulated and observed wind velocities. The simulation was performed in a self-consistent manner by solving the magnetohydrodynamic equations from the photosphere to the solar wind. In high-latitude regions, the simulated solar wind velocity agrees better with the IPS observation than with the classical Wang–Sheeley empirical estimation, both in maximal and minimal activity phases. In mid-latitude regions, the agreement worsens, possibly because of the inaccuracy of the WTD model and/or the magnetic-field extrapolation. Our results indicate that the high-latitude solar wind is likely to be driven by waves and turbulence, and that the physics-based prediction of the solar wind velocity is highly feasible with an improved magnetic-field extrapolation.

Keywords: keyword for arXiv submission

1. INTRODUCTION

The solar wind (Parker 1958; Velli 1994) plays several important roles in astrophysics and heliophysics. It is the principal source of solar angular-momentum loss (Weber & Davis 1967; Sakurai 1985; Kawaler 1988; Réville et al. 2015; Finley et al. 2019, 2020), which results in solar spin-down (Irwin & Bouvier 2009; Gallet & Bouvier 2013; Matt et al. 2015) and weakening of solar magnetic activity over time (Güdel 2007; Brun & Browning 2017; Vidotto 2021). In the space weather forecasting, it is necessary to predict the velocity and spatial structure of the solar wind (including impulsive eruptions) that affect the formation of the co-rotating interaction region (CIR, Smith & Wolfe 1976; Tsurutani et al. 2006) and the arrival time of the coronal mass ejection (CME, Shiota & Kataoka 2016; Wold et al. 2018; Riley & Ben-Nun 2021). Fluctuations in the solar wind

are also important for studying plasma turbulence that extends from the fluid to electron scales (Bruno & Carbone 2013).

One fundamental open question of the solar wind is its heating and acceleration mechanism(s). The classical thermally driven wind model of the solar wind (Parker 1958; Withbroe 1988; Hansteen & Leer 1995) does not account for the observed anti-correlation between the coronal temperature and wind velocity (Geiss et al. 1995; von Steiger et al. 2000), and thus an additional non-thermal acceleration of the solar wind is necessary (Alazraki & Couturier 1971; Belcher 1971; Jacques 1977). In terms of feeding mechanism of the magnetic energy, the solar wind models are classified into two types (Cranmer 2012): wave/turbulence-driven (WTD) models (Suzuki & Inutsuka 2005; Cranmer et al. 2007; Verdini et al. 2010; van der Holst et al. 2014; Réville et al. 2020) and reconnection/loop-opening (RLO) models (Fisk 2003; Antiochos et al. 2011; Higginson et al. 2017).

Several theoretical studies have indicated that the reconnection/loop-opening processes have minor roles

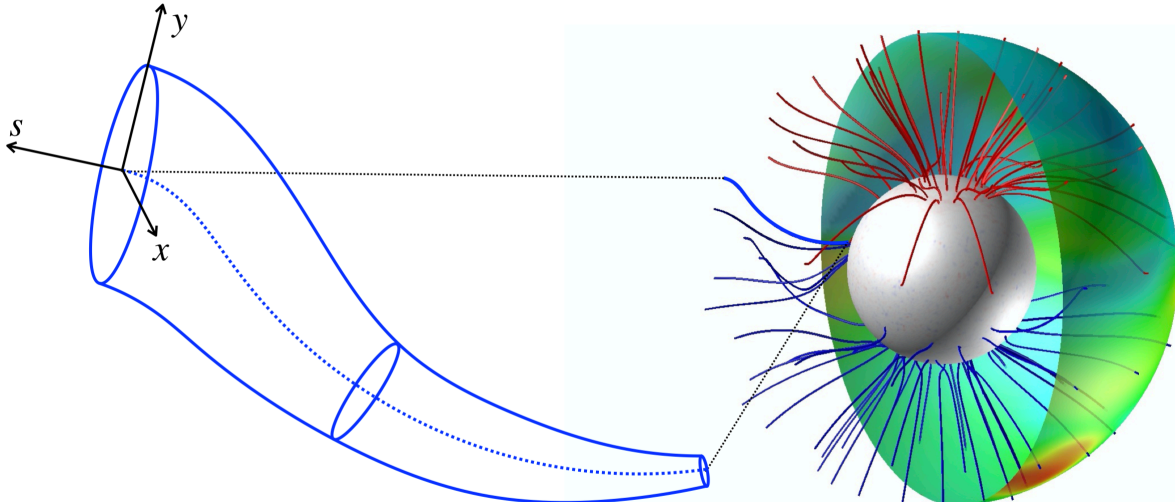


Figure 1. Model overview. Right: 3D view of the photospheric magnetic field measured by GONG and extrapolated field lines with color indicating the polarity. Also shown by the transparent hemisphere is the corresponding IPS measurements of the solar wind velocity. Left: a schematic of the simulation domain. For a given magnetic field line (flux tube), we solve the magnetohydrodynamic equations along the field-aligned coordinate s .

in coronal holes (Cranmer & van Ballegoijen 2010; Lionello et al. 2016). Meanwhile, a recent observational study indicated a non-negligible role of emerging flux (that induces reconnection and loop opening) in the coronal-hole wind (Wang 2020). Models of magnetic switchbacks (Bale et al. 2019; Kasper et al. 2019; Dudok de Wit et al. 2020; Horbury et al. 2020) observed by Parker Solar Probe (Fox et al. 2016) also suggest that interchange reconnection frequently occurs at the base of the coronal hole (Sterling & Moore 2020; Zank et al. 2020; Drake et al. 2021; Magyar et al. 2021), although it should be noted that switchbacks can emerge without interchange reconnection (Squire et al. 2020; Schwadron & McComas 2021; Shoda et al. 2021). The acceleration mechanism(s) of the solar wind, even those from coronal holes, is still (or getting more) controversial.

In this study, we test the wave/turbulence model of the solar wind using interplanetary scintillation (IPS) observations (Hewish et al. 1964; Salpeter 1967), which yields the global structure of the solar wind velocity (Kojima et al. 1998; Tokumaru et al. 2009; Porowski et al. 2021). For this purpose, we perform one-dimensional solar wind simulations for multiple open flux tubes and compare the simulated solar wind velocity with the IPS measurements. An advantage of our model over the previous multiple flux-tube model of the solar wind (MULTI-VP, Pinto & Rouillard 2017) is that we model the solar wind with Alfvén-wave heating and acceleration mechanisms, while MULTI-VP is more practical in

the space weather forecasting because of its small computational cost (Samara et al. 2021). The radial structure of the open magnetic field is required as an input for the simulation and is inferred from the potential-field-source-surface (PFSS) extrapolation of the photospheric magnetic field. In particular, we investigate how accurately the wave/turbulence model predicts the solar wind velocity for a given magnetic field configuration.

The remainder of this paper is organized as follows. The extrapolation of the magnetic field and simulation setting are detailed in Section 2. In Section 3, we first provide an overview of the simulation results and thereafter compare them with the IPS measurements for the activity-minimum and -maximum phases. Finally, the discovery and possible future improvements are discussed in Section 4.

2. MODEL

2.1. Model overview

The overview of the model is shown in Figure 1. The large-scale magnetic field was extrapolated using the PFSS method (Altschuler & Newkirk 1969; Schatten et al. 1969; Shiota et al. 2012). Given the shape (cross-section) and inclination (angle with respect to the vertical direction) of the flux tube, one-dimensional magnetohydrodynamic equations were numerically solved along the flux tube from the photosphere to the solar wind. The simulated velocity was thereafter compared to the IPS observations to test the model accuracy. We de-

scribe the details of the magnetic-field extrapolation and basic equations in Sections 2.2 and 2.3, respectively.

2.2. Background magnetic field

To perform a one-dimensional solar wind simulation, we need to prescribe the field strength B_s and the inclination with respect to the vertical (radial) direction θ_{BR} of the background flux tube. The detailed procedure is described as follows.

First, we extrapolate the magnetic field using the PFSS method. The source surface radius r_{SS} is set to the conventional value of $r_{SS}/R_\odot = 2.5$ (Hoeksema et al. 1983; Wang & Sheeley 1988). The GONG synoptic map (Harvey et al. 1996) is used as the photospheric boundary condition. For simplicity, we ignore the effect of solar rotation, which is unlikely to affect the solar wind velocity (Weber & Davis 1967). For a given set of latitude and longitude at the source surface, we obtained the corresponding field-aligned profiles of the radial distance r^{PFSS} and field strength B^{PFSS} . It is, however, risky to directly adopt the magnetic field extrapolated in this manner. The open magnetic flux obtained from the PFSS method ($r_{SS}/R_\odot = 2.5$) with the GONG magnetogram was found to be three time smaller than the observed value (open-flux problem, see Linker et al. 2017, 2021). This gap is attributed to the missing magnetic flux in the GONG magnetogram and/or the inaccuracy in the PFSS extrapolation. To make the open flux consistent with the in-situ observations, the background magnetic field is defined by the PFSS field multiplied by three:

$$B_s = 3B^{\text{PFSS}}(s), \quad r = r^{\text{PFSS}}(s), \quad (1)$$

where B_s denotes the field strength of the background flux tube, r is the radial distance and s is the field-aligned coordinate. Because the PFSS extrapolation is incapable of describing the magnetic field in the lower atmosphere, Eq. (1) is adopted for $r/R_\odot > 1.02$.

In the lower atmosphere ($1 \leq r/R_\odot \leq 1.02$), although direct observation of the magnetic field is still difficult, flux tubes appear to expand with height in response to an exponential decrease in the ambient gas pressure (Ishikawa et al. 2021). Here, we simply assume that the magnetic field expands to keep the plasma beta nearly constant until the field strength reaches the coronal-base value.

$$B_s(s) = \max \left[B_{s,\text{cb}}, B_{s,\odot} \exp \left(-\frac{r - R_\odot}{2H_{p,\odot}} \right) \right], \quad (2)$$

where $B_{s,\text{cb}}$ denotes the field strength at the coronal base, $B_{s,\odot}$ is the photospheric field strength, and

$H_{p,\odot} = 150$ km is the pressure scale height in the photosphere. Assuming that the pressure scale height is constant in the photosphere and chromosphere, the height distribution of the pressure is given as follows:

$$p(s) \approx p_\odot \exp \left(-\frac{r - R_\odot}{H_{p,\odot}} \right), \quad (3)$$

yielding the plasma beta constant in s :

$$\beta(s) = \frac{8\pi p(s)}{B_s(s)^2} \approx \frac{8\pi p_\odot}{B_{s,\odot}^2} \quad (\text{if } B_s > B_{s,\text{cb}}). \quad (4)$$

Although the actual chromospheric magnetic field could deviate from Eq. (2), we have confirmed that the solar wind velocity is only slightly affected by the formulation of B_s in the lower atmosphere (see Appendix for detail). Therefore, the arbitrary choice of B_s does not significantly affect the conclusion of this work.

We require that the background field strength is continuous. From Eq. (1) adopted in $r/R_\odot > 1.02$, and Eq. (2) adopted in $r/R_\odot \leq 1.02$, we obtain the following condition.

$$B_{s,\text{cb}} = 3 B^{\text{PFSS}} \Big|_{r/R_\odot=1.02}. \quad (5)$$

Although a fraction of the magnetic field in the lower atmosphere should be highly inclined (De Pontieu et al. 2004), we simply assume that the flux tubes are vertical in the lower atmosphere. In terms of r , the vertical magnetic field is represented by

$$r(s) = s, \quad (6)$$

for $1 \leq r/R_\odot \leq 1.02$.

2.3. Basic equations and simulation setting

Given the field-aligned profile of the background flux tube, the one-dimensional MHD equations with gravity, thermal conduction, and radiation are solved along the expanding flux tube. The basic equations are given by

(see Shoda & Takasao 2021, for derivation)

$$\frac{\partial \rho}{\partial t} + \frac{1}{r^2 f} \frac{\partial}{\partial s} (\rho v_s r^2 f) = 0, \quad (7)$$

$$\begin{aligned} \frac{\partial}{\partial t} (\rho v_s) + \frac{1}{r^2 f} \frac{\partial}{\partial s} \left[\left(\rho v_s^2 + p + \frac{\mathbf{B}_\perp^2}{8\pi} \right) r^2 f \right] \\ = \left(p + \frac{1}{2} \rho v_s^2 \right) \frac{d}{ds} \ln(r^2 f) - \rho \frac{GM_\odot}{r^2} \frac{dr}{ds}, \end{aligned} \quad (8)$$

$$\begin{aligned} \frac{\partial}{\partial t} (\rho \mathbf{v}_\perp) + \frac{1}{r^2 f} \frac{\partial}{\partial s} \left[\left(\rho v_s \mathbf{v}_\perp - \frac{B_s \mathbf{B}_\perp}{4\pi} \right) r^2 f \right] \\ = \frac{1}{2} \left(-\rho v_s \mathbf{v}_\perp + \frac{B_s \mathbf{B}_\perp}{4\pi} \right) \frac{d}{ds} \ln(r^2 f) + \rho \mathbf{D}_\perp^v, \end{aligned} \quad (9)$$

$$\begin{aligned} \frac{\partial}{\partial t} \mathbf{B}_\perp + \frac{1}{r^2 f} \frac{\partial}{\partial s} [(v_s \mathbf{B}_\perp - B_s \mathbf{v}_\perp) r^2 f] \\ = \frac{1}{2} (v_s \mathbf{B}_\perp - B_s \mathbf{v}_\perp) \frac{d}{ds} \ln(r^2 f) + \sqrt{4\pi \rho} \mathbf{D}_\perp^b, \end{aligned} \quad (10)$$

$$\begin{aligned} \frac{\partial}{\partial t} e + \frac{1}{r^2 f} \frac{\partial}{\partial s} \left[(e + p_T) v_s - \frac{B_s}{4\pi} (\mathbf{v}_\perp \cdot \mathbf{B}_\perp) \right] \\ = -\rho v_s \frac{GM_\odot}{r^2} \frac{dr}{ds} + Q_{\text{cnd}} + Q_{\text{rad}}, \end{aligned} \quad (11)$$

where

$$\mathbf{v}_\perp = v_x \mathbf{e}_x + v_y \mathbf{e}_y, \quad \mathbf{B}_\perp = B_x \mathbf{e}_x + B_y \mathbf{e}_y, \quad (12)$$

$$p_T = p + \frac{\mathbf{B}_\perp^2}{8\pi}, \quad e = e_{\text{int}} + \frac{1}{2} \rho v^2 + \frac{\mathbf{B}_\perp^2}{8\pi}. \quad (13)$$

The term $\mathbf{D}_\perp^{v,b}$ denotes the phenomenological turbulent dissipation term (Shoda et al. 2018), which is given by

$$D_{x,y}^v = -\frac{c_d}{4\lambda_\perp} (|z_{x,y}^+| z_{x,y}^- + |z_{x,y}^-| z_{x,y}^+), \quad (14)$$

$$D_{x,y}^b = -\frac{c_d}{4\lambda_\perp} (|z_{x,y}^+| z_{x,y}^- - |z_{x,y}^-| z_{x,y}^+), \quad (15)$$

where $z_{x,y}^\pm = v_{x,y} \mp B_{x,y} / \sqrt{4\pi\rho}$. The perpendicular correlation length is assumed to be proportional to the flux-tube radius.

$$\lambda_\perp = \lambda_{\perp,\odot} \frac{r}{R_\odot} \sqrt{\frac{f}{f_\odot}}, \quad (16)$$

where we set the photospheric correlation length to $\lambda_{\perp,\odot} = 1,000$ km. Q_{cnd} and Q_{rad} represent the conduction heating per unit volume and radiative heating per unit volume, respectively.

Assuming that the gas is composed of hydrogen, an equation of state with partially ionized hydrogen is used to connect the pressure, density, and temperature. Considering the latent heat, the internal energy density is given by

$$e_{\text{int}} = \frac{p}{\gamma - 1} + \chi_H n_H I_H, \quad (17)$$

where ξ_H is the ionization degree of hydrogen, n_H is the number density of hydrogen atom, and $I_H = 13.6$ eV is the hydrogen ionization potential. To obtain ξ_H , we use an approximated Saha-Boltzmann equation. The detailed procedure is described in Shoda & Takasao (2021).

There are effects from partial ionization other than latent heat. One of them is the enhanced dissipation of magnetic field, the ambipolar diffusion, which is known to affect the propagation of high-frequency Alfvén waves in the chromosphere (Khomenko et al. 2014). Such high-frequency waves are likely to be generated in a multi-dimensional system (see discussion in Cally & Khomenko 2018). Because the system is one-dimensional in this work, the effect of partial ionization is not considered and remains to be seen.

The conductive heating is implemented in terms of conductive flux q_{cnd} by

$$Q_{\text{cnd}} = -\frac{1}{r^2 f} \frac{\partial}{\partial s} (q_{\text{cnd}} r^2 f). \quad (18)$$

The Spitzer-Härm flux (Spitzer & Härm 1953) is employed as the conductive flux. To speed up the calculation without loss of reality, we quench the conductive flux in the distant region where ρ is smaller than the critical value ρ_{sw} . The formulation of q_{cnd} is given by

$$q_{\text{cnd}} = -\kappa_{\text{SH}} T^{5/2} \frac{\partial T}{\partial s} \min \left(1, \frac{\rho}{\rho_{\text{sw}}} \right), \quad (19)$$

where $\kappa_{\text{SH}} = 1.0 \times 10^{-6}$ erg cm K^{-7/2}. We set $\rho_{\text{sw}} = 10^{-20}$ g cm⁻³.

The radiative heating is implemented as follows.

$$Q_{\text{rad}} = -\frac{1}{\tau_{\text{rad}}} (e_{\text{int}} - e_{\text{int}}^{\text{ref}}) (1 - \xi_{\text{rad}}) + n_e n_H \Lambda(T) \xi_{\text{rad}}, \quad (20)$$

where

$$\tau_{\text{rad}} = 0.1 \text{ s} \sqrt{\frac{\rho_\odot}{\rho}}, \quad \xi_{\text{rad}} = \min \left[1, \exp \left(-10 \frac{p}{p_\odot} \right) \right], \quad (21)$$

where the subscript \odot denotes the value at the photosphere. The term $e_{\text{int}}^{\text{ref}}$ denotes the reference internal energy corresponding to the reference temperature T^{ref} , and $\Lambda(T)$ is the optically-thin radiative loss function. We set $T^{\text{ref}} = T_\odot$. To define $\Lambda(T)$ over a wide temperature range, we smoothly bridge the chromospheric (Goodman & Judge 2012) and coronal loss functions from the CHIANTI atomic database version 10 (Dere et al. 1997; Del Zanna et al. 2021) following Iijima (2016) (see Shoda & Takasao (2021) for details).

2.4. Simulation domain and boundary condition

The simulation domain extends from the photosphere and is aligned with the background magnetic field. The radial distance of the outer boundary depends on the inclination of the magnetic field, but is always beyond $30R_\odot$. The grid size Δs is fixed to the minimum value Δs_m below the prescribed critical height s_{ge} and expands in s until it reaches the maximum value Δs_M . Letting s_i and Δs_i be the position and size of the i -th grid, respectively, we define Δs_i as follows.

$$\Delta s_i = \max \left[\Delta s_m, \min \left[\Delta s_M, \Delta s_m + \frac{2\varepsilon_{ge}(s_{i-1} - s_{ge})}{2 + \varepsilon_{ge}} \right] \right],$$

$$s_i = s_{i-1} + \frac{1}{2} (\Delta s_{i-1} + \Delta s_i), \quad s_0 = R_\odot \quad (22)$$

where we set

$$\begin{aligned} \Delta s_m &= 20 \text{ km}, & \Delta s_M &= 2000 \text{ km}, \\ s_{ge} &= 1.04R_\odot, & \varepsilon_{ge} &= 0.01. \end{aligned}$$

At the outer boundary, because the solar wind becomes supersonic and super-Alfvénic, any MHD waves propagate only in the outward direction. For this reason, we impose the free boundary conditions as

$$\left. \frac{\partial \rho}{\partial s} \right|_{\text{out}} = 0, \quad \left. \frac{\partial \mathbf{v}}{\partial s} \right|_{\text{out}} = 0, \quad \left. \frac{\partial \mathbf{B}_\perp}{\partial s} \right|_{\text{out}} = 0, \quad (23)$$

where the subscript ‘‘out’’ denotes the value at the outer boundary. Because heat can propagate backward against the supersonic flow by thermal conduction, it would be risky to impose a free boundary condition for p or e_{int} . Instead, we impose the boundary condition for e_{int} as follows:

$$1e_{\text{int}} \propto r^{-1/2} \quad (r \geq r_{\text{out}}). \quad (24)$$

At the inner boundary, the temperature is fixed to the solar effective temperature.

$$T_\odot = 5.77 \times 10^3 \text{ K}, \quad (25)$$

where the subscript \odot denotes the value at the inner boundary. Some solar observations reveal that the photospheric magnetic fields are localized in kilo-Gauss patches (Keller et al. 2004; Tsuneta et al. 2008). We therefore fix the photospheric field strength to

$$B_{s,\odot} = 1.34 \times 10^3 \text{ G}. \quad (26)$$

To excite upward longitudinal waves at the bottom boundary, we impose the time-dependent boundary conditions for ρ and v_s as follows:

$$\rho_\odot = \overline{\rho_\odot} \left(1 + \frac{\delta v_\odot}{a_\odot} \right), \quad v_{s,\odot} = \delta v_{s,\odot}, \quad (27)$$

where $\delta v_{s,\odot}$ denotes the longitudinal velocity fluctuation at the photosphere. $\overline{\rho_\odot}$ represents the time-averaged mass density, and a_\odot is the sound speed in the photosphere, which are given, respectively, by

$$\overline{\rho_\odot} = 1.88 \times 10^{-7} \text{ g cm}^{-3}, \quad a_\odot = 8.91 \text{ km s}^{-1}. \quad (28)$$

The transverse fluctuations are provided in terms of Elsässer variables defined by

$$\mathbf{z}_\perp^\pm = \mathbf{v}_\perp \mp \frac{\mathbf{B}_\perp}{\sqrt{4\pi\rho}}. \quad (29)$$

The free boundary condition is imposed on the inward Elsässer variables

$$\left. \frac{\partial \mathbf{z}_\perp^-}{\partial s} \right|_\odot = 0. \quad (30)$$

For the upward Elsässer variables, the time-dependent boundary condition is imposed to excite Alfvén waves at the photosphere.

$$z_{x,\odot}^+ = 2\delta v_{x,\odot}, \quad z_{y,\odot}^+ = 2\delta v_{y,\odot} \quad (31)$$

The velocity fluctuations are given in terms of broadband fluctuation by

$$\delta v_{s,x,y,\odot} \propto \sum_{i=0}^N \sin(2\pi f^i t + \phi_{s,x,y}^i) / \sqrt{f^i}, \quad (32)$$

$$f^i = \frac{(N-i)f_{\text{min}} + if_{\text{max}}}{N}, \quad (33)$$

where $\phi_{s,x,y}^i$ represents a random phase function, $N+1$ is the total number of modes, and

$$f_{\text{min}} = 1.00 \times 10^{-3} \text{ Hz}, \quad f_{\text{max}} = 1.00 \times 10^{-2} \text{ Hz}, \quad (34)$$

are the minimum and maximum wave frequencies. In this study, we set $N = 100$. The root-mean-squared amplitudes of $\delta v_{s,x,y,\odot}$ were tuned to 0.4 km s^{-1} , that is,

$$\sqrt{\overline{\delta v_{s,x,y,\odot}^2}} = 0.4 \text{ km s}^{-1}, \quad (35)$$

where the overline denotes the time averaging.

3. RESULT

3.1. Radial structure of the simulated solar wind

Clarifying the detailed physical mechanism of the solar wind heating and acceleration is not the main scope of this study (see, for instance, Shoda et al. 2018, 2019, for a detailed discussion of the physical mechanism). Rather than detailed analyses, we show some examples of the radial structure of the simulated solar wind to grasp an overview of the simulation results.

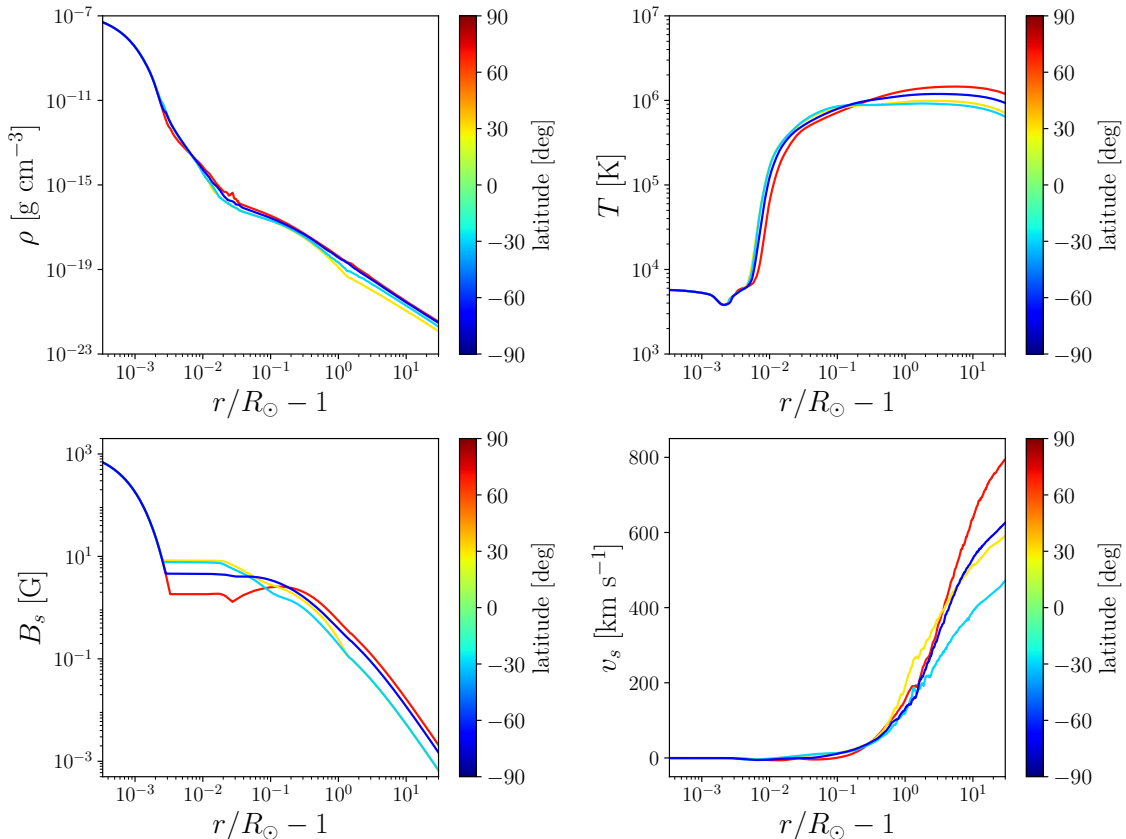


Figure 2. Time-averaged radial structures of the simulated solar wind for CR 2218 (minimal activity phase). The four panels show the mass density (ρ , left top), temperature (T , right top), background magnetic field (B_s , left bottom), and field-aligned velocity (v_s , right bottom), respectively. The line colors indicate the corresponding latitudes (70° , 30° , -30° , -70°) at the source surface. The longitude is fixed to 300° .

Figure 2 shows the time-averaged radial profiles of the simulated solar wind for Carrington rotation (CR) 2218 in which the solar activity was close to the minimum phase. The four lines correspond to 70° , 30° , -30° , and -70° in terms of latitude, as indicated by the line color. The longitude is fixed to 300° . Higher-/lower-speed winds are found in higher/lower latitudes, which is consistent with the observed latitudinal structure in the solar minimum (McComas et al. 2003).

Observing closely the temperature profiles (right-top panel), noticeable differences between fast and slow winds are present. Near the base of the corona ($r/R_\odot - 1 \leq 0.1$), slower winds (yellow and cyan) were hotter than faster winds (red and blue). This relationship is reversed beyond the wind acceleration region ($r/R_\odot - 1 \geq 1$). This behavior is consistent with the fact that the fast solar wind exhibits a larger in-situ proton temperature and smaller freezing-in (coronal base) electron temperature than the slow solar wind (see Cranmer et al. 2017, and references there in).

The relation between the wind velocity and magnetic field is shown in the bottom two panels of Figure 2. The field strength of the faster wind is smaller near the coronal base ($r/R_\odot - 1 \leq 0.1$), but larger in the solar wind ($r/R_\odot - 1 \geq 1$). In terms of the expansion factor, the simulation results imply that a small expansion of flux tube yields a fast solar wind. This relation is consistent with the classical observational trend (Wang & Sheeley 1990; Arge & Pizzo 2000), although the role of expansion factor is recently questioned (Riley et al. 2015).

In brief, our model reproduces 1. the latitudinal distribution of the wind speed, 2. the relationship between the coronal/wind temperature and wind speed, and 3. the inverse correlation between the expansion factor and wind speed. These agreements validate the WTD model in that it accounts for the observed qualitative behavior of the solar wind. To more quantitatively test the model, in the following sections, we compare the simulation results with the IPS measurements.

3.2. Solar wind observation with the IPS

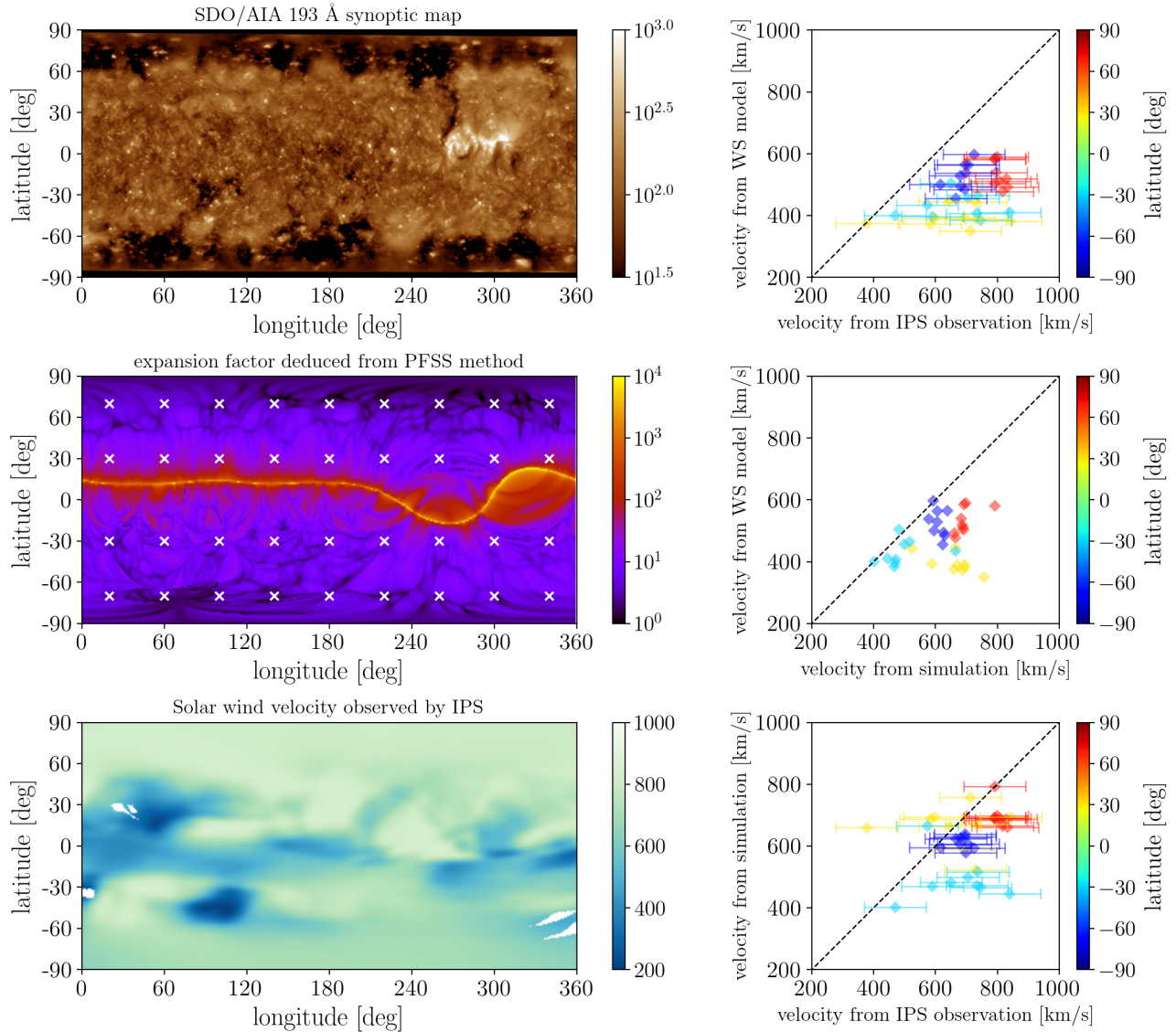


Figure 3. Overview of CR 2218 results. Left-top: synoptic map constructed from SDO/AIA 193 Å observation. Left-middle: flux-tube expansion factor at the source surface ($r = r_{SS}$) deduced from the PFSS extrapolation. We use $r_{SS}/R_{\odot} = 2.5$. Left-bottom: solar wind velocity measured by IPS technique. Right panels: scattered plots showing the correlations between v_{SIM} , v_{WS} , and v_{IPS} . One symbol corresponds to one simulation run, and the color represents the latitude of the wind. The error in v_{IPS} was fixed at 100 km s^{-1} .

The IPS is a radio-scattering phenomenon caused by turbulence in the solar wind. We used the IPS data taken by the Institute for Space-Earth Environmental Research (ISEE), Nagoya University (Tokumaru et al. 2011), which is composed of three radio telescopes at 327 MHz. The solar wind speed is derived by the cross-correlations of the IPS data between the three stations. The global distribution of the solar wind is derived by projecting the solar wind speed data onto the source surface using the tomography method (Jackson et al. 1998; Kojima et al. 1998), which has been recently im-

proved by Tokumaru et al. (2021). The tomography method excludes transient phenomena such as coronal mass ejections that are also detected by IPS observations (for instance, Iwai et al. 2019, 2021). Therefore, the tomography method derives the solar wind velocity of the background solar wind at a steady state.

The root-mean-squared discrepancy between the IPS and the in-situ measurement is typically $100\text{--}150 \text{ km s}^{-1}$. The spatial resolution of the IPS data on the synoptic map is approximately 15° . Hence, we averaged the derived IPS data within the $15^{\circ} \times 15^{\circ}$ region and

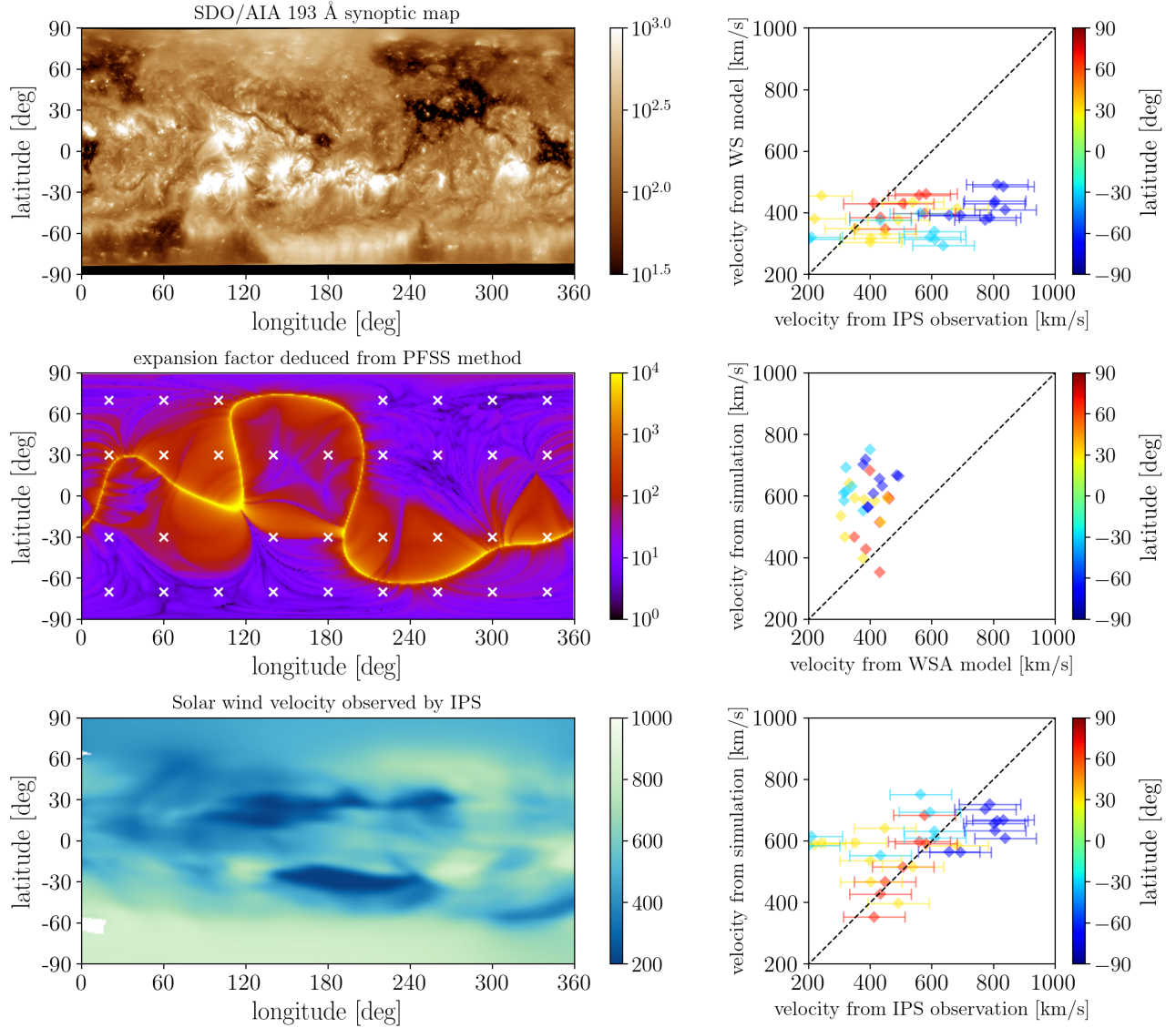


Figure 4. Same as Figure 3 but for CR 2169.

recognized it as a typical solar wind speed. Note that this low resolution of the solar wind map could create an artificial middle-speed wind around the boundary between the fast and slow wind regions, even if the solar wind would be a bi-modal fast and slow wind structure. Therefore, the solar wind speed close to the HCS may have a larger error.

3.3. Solar wind in an inactive phase (CR 2218)

Carrington rotation (CR) 2218 is half a year before the end of the solar cycle 24 in which the monthly averaged relative sunspot number is 1.2, and behaves as a typical phase of the minimal activity. Because the IPS observation and its tomographic analysis provide the nearly full solar wind velocity distribution on the Carrington map,

we focus on CR 2218 as an example of a magnetically inactive phase.

Left panels in Figure 3 show the synoptic maps of the SDO/AIA 193 image (top), the expansion factor f_{exp} deduced from the PFSS method, and the solar wind velocity measured by the IPS observation projected on the source surface ($r/R_{\odot} = 2.5$). The AIA synoptic image is made from the open dataset by Hamada et al. (2020). The simulations were performed for the selected points indicated by the white crosses in the f_{exp} maps. A low level of magnetic activity is observed from the large coronal holes developed at high latitudes (observed in the AIA image) and the current sheet (indicated by the large- f_{exp} region) remaining at low latitudes. As a typi-

cal structure of the solar wind in the activity-minimum, high- and low-latitude regions are dominated by fast and slow solar winds, respectively (as seen in the IPS map).

The three right in Figure 3 show the correlations between the three solar wind velocities: v_{SIM} , v_{WS} , and v_{IPS} . v_{SIM} denotes the wind speed from the simulation, which is defined by the time-averaged field-aligned velocity at $r/R_{\odot} = 30$, that is,

$$v_{\text{SIM}} = \overline{v_s}|_{r/R_{\odot}=30}, \quad (36)$$

where the overline denotes the time averaging. v_{WS} is the wind speed predicted by the empirical Wang–Sheeley model (Wang & Sheeley 1990). In this study, we use the relation by Arge & Pizzo (2000), that is,

$$v_{\text{WS}} = 267.5 + \frac{410.0}{f_{\text{exp}}^{2/5}} \text{ km s}^{-1}, \quad (37)$$

where f_{exp} denotes the expansion factor. v_{IPS} denotes the IPS measurement of the wind speed.

The three scattered plots show the following results.

1. The Wang–Sheeley empirical model (v_{WS}) is systematically lower than the observed velocity (v_{IPS}). The deviation between the two is larger for high-latitude cases.
2. The simulated wind velocity (v_{SIM}) exhibits a better agreement with the IPS measurement (v_{IPS}) than with the Wang–Sheeley empirical model (v_{WS}). The agreement is particularly good in high-latitude cases.

The Wang–Sheeley model shows better performance in the lower-latitude region, and it is a natural consequence because the model is calibrated by near-Earth observations. From these scattered plots, our model was found to reproduce the observed wind velocity with a better accuracy than the Wang–Sheeley model, at least in high-latitude regions. We investigate whether this trend is also found in the activity-maximum phase in the following section.

3.4. Solar wind in an active phase (CR 2169)

Carrington Rotation (CR) 2169, beginning on October 4th and ending on October 31st in 2015, is 1.5 years after the sunspot-number maximum in solar cycle 24 with the monthly averaged relative sunspot number of 63.6. Because the global structure of the solar wind is obtained by the IPS during this rotation, we focus on CR 2169 as an example of a magnetically active phase.

Figure 4 shows the observation and simulation results in the same format as Figure 3 but for CR 2169. Unlike CR 2218, a high level of magnetic activity is observed in

the AIA coronal image with several bright structures at low latitudes. As seen in the IPS map, a fraction of the northern polar region is dominated by slow solar wind, which is also typical of the magnetically active phase.

As shown in Figure 3, the simulation points are indicated by the white crosses in the f_{exp} map. Simulations at (longitude, latitude) = (100°, -30°), (140°, 70°), and (180°, 70°) are not performed because, in these cases, the PFSS extrapolation yields unrealistic discontinuities in the field strength near the source surface.

The scatter plots on the right-hand side of Figure 4 exhibit a similar trend to that shown in 3. The Wang–Sheeley relation tends to predict slower wind speeds than the IPS measurement, while the agreement is much better between the simulation and IPS, particularly in the high-latitude region. In contrast to CR 2218, in which both polar regions are dominated by fast solar wind, a fraction of the northern polar region is covered by the slow solar wind. Interestingly, the slow solar wind in the northern polar region is reproduced by our simulation, as shown by the red symbols in the right-bottom panel of Figure 4.

In the mid-latitude cases, the Wang–Sheeley relation and simulation exhibited opposite trends with respect to the IPS measurement. The Wang–Sheeley relation tends to underestimate the wind velocity, whereas the simulation tends to overestimate it. The two methods yield a similar level of root-mean-squared deviation from the IPS measurements. As in CR 2218, we find that the Wang–Sheeley relation performs better in the lower-latitude regions.

3.5. Performance in the wind velocity prediction

To evaluate the performance of the Wang–Sheeley relation and simulation in the wind velocity prediction, we calculated the root-mean-squared error Δv_{rms} with respect to the IPS measurement as follows.

$$\Delta v_{\text{rms}} = \sqrt{\frac{1}{N} \sum_{i=1}^N (v_{\text{WS, SIM}}^i - v_{\text{IPS}}^i)^2}, \quad (38)$$

where N denotes the total number of simulation runs and the superscript i denotes the i -th simulation run. Δv_{rms} is calculated separately for high-latitude, mid-latitude, and all runs for each CR. The results of the error calculation are summarized in Table 1.

In high-latitude cases, the root-mean-squared error of the simulation is $\Delta v_{\text{rms}} \approx 100 \text{ km s}^{-1}$, approximately in the same magnitude as the error in the IPS observations. Interestingly, CR 2169 and 2218 yielded nearly the same value of the simulation error despite the different levels of magnetic activity. The Wang–Sheeley relation yields

Carrington Rotation	velocity model	Δv_{rms} [km s ⁻¹] (high-lat cases)	Δv_{rms} [km s ⁻¹] (mid-lat cases)	Δv_{rms} [km s ⁻¹] (all cases)
CR 2169 (active phase)	simulation	112.8	171.4	135.2
CR 2169 (active phase)	Wang-Sheeley relation	277.5	156.1	243.8
CR 2218 (inactive phase)	simulation	103.0	185.0	149.7
CR 2218 (inactive phase)	Wang-Sheeley relation	227.7	278.4	254.3

Table 1. This table summarizes the root-mean-squared errors of the solar wind velocity Δv_{rms} for the simulation and Wang-Sheeley relation. The value of Δv_{rms} is calculated for high-latitude cases (latitude = $\pm 70^\circ$), mid-latitude cases (latitude = $\pm 30^\circ$), and all cases (latitude = $\pm 30^\circ$, $\pm 70^\circ$).

a much larger error, typically $\Delta v_{\text{rms}} \approx 250 \text{ km s}^{-1}$, with a larger error found in the active phase (CR 2169).

In mid-latitude cases, the accuracy of the simulation decreases, as already discussed in Sections 3.3 and 3.4. In CR 2169, the Wang-Sheeley relation exhibits better performance than the simulation. In contrast, in CR 2218, the simulation is still more accurate than the Wang-Sheeley relation.

The all-case root-mean-squared errors are $\Delta v_{\text{rms}} \approx 140 \text{ km s}^{-1}$ for the simulation, and $\Delta v_{\text{rms}} \approx 250 \text{ km s}^{-1}$ for the Wang-Sheeley relation. From the data provided here, it would be risky to conclude that the simulation is more capable of predicting the wind velocity than the Wang-Sheeley relation. To discuss the performance of the solar wind prediction, we need to consider a large number of CRs with a range of magnetic activity. The Wang-Sheeley relation should also be calibrated to maximize its performance, because its best-fit model varies over time (Riley et al. 2015). Instead, we conclude that the Alfvén-wave model of the solar wind has the potential to predict the solar wind velocity in a first-principle manner, at least in high-latitude regions.

4. SUMMARY AND DISCUSSION

In this study, we test the theoretical (wave/turbulence-driven, WTD) model of the solar wind using IPS observations. Along background field lines inferred by the PFSS method, we directly solved the MHD equations from the photosphere to the solar wind. The simulated solar wind velocity was directly compared with the IPS measurements to validate the model performance.

Regardless of the activity level, the WTD model of the solar wind accurately reproduces the observed wind velocity at high latitudes, with a typical root-mean-squared error of 100 km s^{-1} . Given that the typical error in the IPS measurement is $100 - 150 \text{ km s}^{-1}$, we conclude that the WTD model captures the structure

of high-latitude solar wind. In terms of the acceleration mechanism, our results indicate that the high-latitude solar wind is accelerated by Alfvén waves, even in the activity maximum phase. Indeed, the slow solar wind observed in the northern polar region of CR 2169 was well reproduced by the model.

In the mid-latitude cases, the WTD model becomes less accurate, with a typical root-mean-squared error of 180 km s^{-1} . There are three possible reasons for this reduction in accuracy.

First, physical mechanisms other than Alfvén-wave heating and acceleration work in the lower-latitude regions. One promising mechanism for the additional energy release is interchange reconnection (Fisk 2003; Antiochos et al. 2011). Indeed, some solar observations indicate the presence of localized outflows near the edge of active regions (Sakao et al. 2007; Harra et al. 2008; Brooks & Warren 2011; Brooks et al. 2020, 2021), which are found to feed a non-negligible fraction of mass flux into the solar wind (Brooks et al. 2015). To improve the model accuracy, reconnection-driven energy release must be considered (Lionello et al. 2016; Cranmer 2018) as well as granulation-driven Alfvén waves (Wang 2020).

Second, magnetic-field extrapolation could be inaccurate in the lower-latitude region. Although the PFSS method is found to reproduce a large-scale magnetic field without a large numerical cost (Riley et al. 2006), it is no longer validated near the current sheets that tend to appear in mid- to low-latitude regions. A possible improvement is to adopt the Schatten current sheet model (SCS, Schatten 1971), which is found to account for the latitudinal dependence of the interplanetary magnetic field beyond the PFSS model (Wang & Sheeley 1995). We note that, when connecting the PFSS and SCS models, careful treatment is required to reduce the discontinuity in the magnetic field (McGregor et al. 2008; Reiss et al. 2020). Another factor that affects the accuracy of magnetic field extrapolation is the value of the source

surface radius r_{SS} . Although we adopt the conventional value of r_{SS} ($r_{\text{SS}}/R_{\odot} = 2.5$, [Hoeksema et al. 1983](#)), a recent *Parker Solar Probe* observation reveals that the source surface can be much closer ([Badman et al. 2020](#)). The photospheric magnetogram can also be improved, from GONG observations to the data-assimilated flux-transport model (ADAPT, [Arge et al. 2010](#)). In fact, the open-flux problem could be (partly) solved by adding magnetic flux in the polar region ([Riley et al. 2019](#)), which indicates that the observed magnetic field in the polar region is still inaccurate. These uncertainties need to be discussed quantitatively in future.

Finally, there is also a possibility that the spatial resolution of the IPS observation was not sufficient to resolve the complicated solar wind source region in the active phase case. The improved IPS observation could give a better spatial resolution of the tomographic map in future.

In spite of the limitations mentioned above, the high-latitude solar wind is well reproduced by the physics-based WTD model. In addition to the novel validation of the WTD model, this study opens the possibility of a physics-based photosphere-wind connection beyond the current transition region-wind connection ([van der Holst et al. 2014](#); [Usmanov et al. 2018](#)). Most of the current

space-weather models employ the empirical solar wind velocity ([Riley et al. 2001, 2015](#)) at the inner boundary. ([Odstrcil 2003](#); [Shiota et al. 2014](#); [Cash et al. 2015](#); [Wold et al. 2018](#)). Improvements of this work could lead to the theoretical validation of the empirical models (e.g. WSA model, [Arge et al. 2004](#); [Riley et al. 2015](#)), and ideally, improved forecasting of space weather.

Numerical computations were carried out on the Cray XC50 at the Center for Computational Astrophysics (CfCA), National Astronomical Observatory of Japan. IPS observations were performed under the solar wind program of the Institute for Space-Earth Environmental Research, Nagoya University. M.S. is supported by a Grant-in-Aid for Japan Society for the Promotion of Science (JSPS) Fellows and by the NINS program for cross-disciplinary study (grant Nos. 01321802 and 01311904) on Turbulence, Transport, and Heating Dynamics in Laboratory and Solar/ Astrophysical Plasmas: “SoLaBo-X.” K.I. is supported by JSPS KAKENHI grant Nos. 19K22028 and 21H04517. D.S. is supported by JSPS KAKENHI grant Nos. 19K23472 and 21H04492. This work made use of matplotlib, a Python library for publication quality graphics ([Hunter 2007](#)), and NumPy ([van der Walt et al. 2011](#)).

APPENDIX

A. UNCERTAINTY IN THE CHROMOSPHERIC MAGNETIC FIELD

In all the simulation runs displayed above, we have assumed that the magnetic field expands to keep the plasma beta nearly unity from the photosphere to the chromosphere (see Eq (2)). This assumption is validated by neither simulation nor observation, and thus, we should discuss how the solar wind speed is affected by the choice of the magnetic-field profile in the lower atmosphere. For this purpose, we have performed a parameter survey on the chromospheric magnetic field for a fixed latitude, longitude, and Carrington rotation. Specifically, we focus on (longitude, latitude) = (20°, 20°) in CR 2218.

As in Eq (2), we assume that the magnetic field exponentially decreases as a function of height until it reaches the basal (coronal) value.

$$B_s(s) = \max \left[B_{s,\text{cb}}, B_{s,0} \exp \left(-\frac{r - R_{\odot}}{c_{\text{mag}} H_{\odot}} \right) \right]. \quad (\text{A1})$$

We note that, letting $B_{s,0} = B_{s,\odot} = 1340$ G and $c_{\text{mag}} = 2.0$, Eq. (A1) is equivalent to Eq (2). We have performed a series of simulation with respect to $B_{s,0}$ and c_{mag} , the list of which is shown in Table 2.

Figure 5 shows the overview of this survey. The three panels display the time-averaged radial profiles of B_s (left), $\beta = 8\pi p/B_s^2$ (middle), and v_s (right), respectively. The black solid line corresponds to the fiducial case ($B_{s,0} = 1340$ G and $c_{\text{mag}} = 2.0$), in which $\beta \approx 1$ in the lower atmosphere ($r/R_{\odot} - 1 < 10^{-3}$), as seen in the middle panel. The two dotted lines (red and blue) are the cases with $B_{s,0} = 1340$ G but different c_{mag} values. We note that the blue and red lines correspond to the high- and low-beta chromospheres, respectively. In spite of substantial differences in the chromospheric magnetic field, the solar wind velocity remains similar. The two dashed lines (orange and green) are the cases with smaller $B_{s,0}$ ($B_{s,0} = 335$ G). Again, although the profiles in the plasma beta is significantly different from the fiducial case, the resultant solar wind velocity is similar. These results indicate that the chromospheric magnetic field has a weak influence on the solar wind velocity.

$B_{s,0}$ [G]	c_{mag}	v_r [km s $^{-1}$]	\dot{M}_w [M_\odot yr $^{-1}$]
1340	2.0	692	1.78×10^{-14}
1340	1.5	658	1.51×10^{-14}
1340	2.5	745	1.49×10^{-14}
335	2.0	611	2.01×10^{-14}
335	3.0	620	2.38×10^{-14}

Table 2. List of the simulation runs in this survey. The wind velocity (v_r) and the mass-loss rate ($\dot{M}_w = 4\pi r^2 \rho v_r$) are measured at $r/R_\odot = 30$ and time averaged.

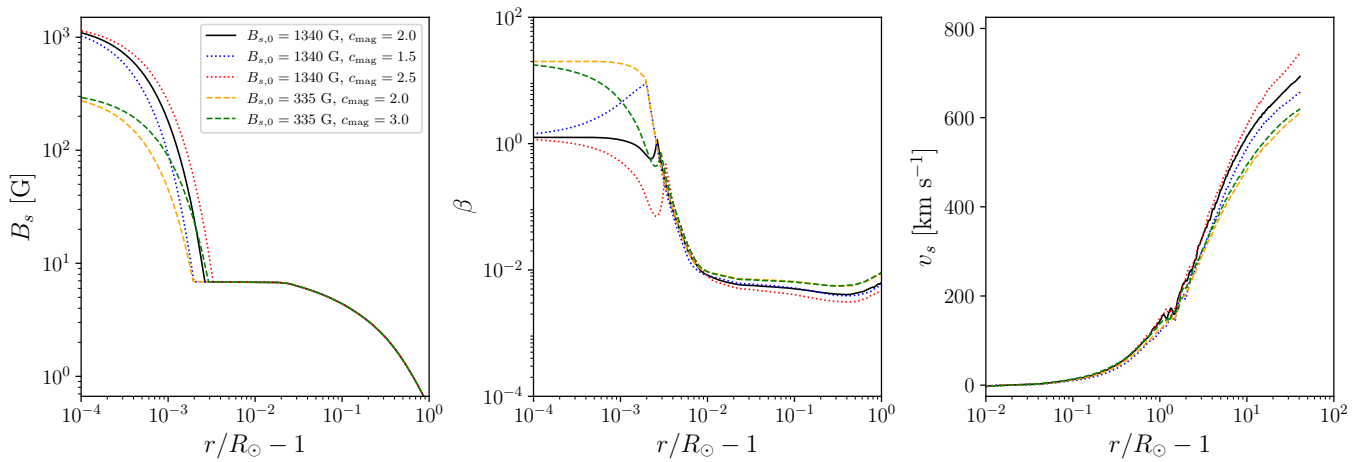


Figure 5. Time-averaged radial profiles of the background magnetic field B_s (left), plasma beta $\beta = 8\pi p/B_s^2$ (middle), and tube-aligned velocity (right). The black solid line corresponds to the fiducial case ($B_{s,0} = 1340$ G and $c_{\text{mag}} = 2.0$). The dotted lines show the cases with the same photospheric field strength ($B_{s,0} = 1340$ G) and the different values of c_{mag} (blue: $c_{\text{mag}} = 1.5$, red: $c_{\text{mag}} = 2.5$). The dashed lines show the cases with the smaller photospheric field strength (orange: $B_{s,0} = 335$ G and $c_{\text{mag}} = 2.0$, green: $B_{s,0} = 335$ G and $c_{\text{mag}} = 3.0$).

To see more quantitatively the uncertainty that comes from the chromospheric magnetic field, Table 2 shows the values of the solar wind velocity v_r and the mass-loss rate $\dot{M}_w = 4\pi r^2 \rho v_r$, both measured at $r/R_\odot = 30$. According to the table, the wind velocity typically has an uncertainty of ± 80 km s $^{-1}$ that comes from the choice of the chromospheric magnetic field. In terms of mass-loss rate, the uncertainty is as large as $\sim 50\%$, much larger than that of the wind velocity. To conclude, the solar wind velocity is weakly affected by the chromospheric magnetic field, while it has a larger impact on the mass flux.

REFERENCES

- Alazraki, G., & Couturier, P. 1971, A&A, 13, 380
- Antiochos, S. K., Mikić, Z., Titov, V. S., Lionello, R., & Linker, J. A. 2011, ApJ, 731, 112, doi: 10.1088/0004-637X/731/2/112
- Altschuler, M. D., & Newkirk, G. 1969, SoPh, 9, 131, doi: 10.1007/BF00145734

- Arge, C. N., Henney, C. J., Koller, J., et al. 2010, in American Institute of Physics Conference Series, Vol. 1216, Twelfth International Solar Wind Conference, ed. M. Maksimovic, K. Issautier, N. Meyer-Vernet, M. Moncuquet, & F. Pantellini, 343–346, doi: [10.1063/1.3395870](https://doi.org/10.1063/1.3395870)
- Arge, C. N., Luhmann, J. G., Odstreil, D., Schrijver, C. J., & Li, Y. 2004, *Journal of Atmospheric and Solar-Terrestrial Physics*, 66, 1295, doi: [10.1016/j.jastp.2004.03.018](https://doi.org/10.1016/j.jastp.2004.03.018)
- Arge, C. N., & Pizzo, V. J. 2000, *J. Geophys. Res.*, 105, 10465, doi: [10.1029/1999JA000262](https://doi.org/10.1029/1999JA000262)
- Badman, S. T., Bale, S. D., Martínez Oliveros, J. C., et al. 2020, *ApJS*, 246, 23, doi: [10.3847/1538-4365/ab4da7](https://doi.org/10.3847/1538-4365/ab4da7)
- Bale, S. D., Badman, S. T., Bonnell, J. W., et al. 2019, *Nature*, 576, 237, doi: [10.1038/s41586-019-1818-7](https://doi.org/10.1038/s41586-019-1818-7)
- Belcher, J. W. 1971, *ApJ*, 168, 509, doi: [10.1086/151105](https://doi.org/10.1086/151105)
- Brooks, D. H., Harra, L., Bale, S. D., et al. 2021, *ApJ*, 917, 25, doi: [10.3847/1538-4357/ac0917](https://doi.org/10.3847/1538-4357/ac0917)
- Brooks, D. H., Ugarte-Urra, I., & Warren, H. P. 2015, *Nature Communications*, 6, 5947, doi: [10.1038/ncomms6947](https://doi.org/10.1038/ncomms6947)
- Brooks, D. H., & Warren, H. P. 2011, *ApJL*, 727, L13, doi: [10.1088/2041-8205/727/1/L13](https://doi.org/10.1088/2041-8205/727/1/L13)
- Brooks, D. H., Winebarger, A. R., Savage, S., et al. 2020, *ApJ*, 894, 144, doi: [10.3847/1538-4357/ab8a4c](https://doi.org/10.3847/1538-4357/ab8a4c)
- Brun, A. S., & Browning, M. K. 2017, *Living Reviews in Solar Physics*, 14, 4, doi: [10.1007/s41116-017-0007-8](https://doi.org/10.1007/s41116-017-0007-8)
- Bruno, R., & Carbone, V. 2013, *Living Reviews in Solar Physics*, 10, 2, doi: [10.12942/lrsp-2013-2](https://doi.org/10.12942/lrsp-2013-2)
- Cally, P. S., & Khomenko, E. 2018, *ApJ*, 856, 20, doi: [10.3847/1538-4357/aaaf6a](https://doi.org/10.3847/1538-4357/aaaf6a)
- Cash, M. D., Biesecker, D. A., Pizzo, V., et al. 2015, *Space Weather*, 13, 611, doi: [10.1002/2015SW001232](https://doi.org/10.1002/2015SW001232)
- Cranmer, S. R. 2012, *SSRv*, 172, 145, doi: [10.1007/s11214-010-9674-7](https://doi.org/10.1007/s11214-010-9674-7)
- . 2018, *ApJ*, 862, 6, doi: [10.3847/1538-4357/aac953](https://doi.org/10.3847/1538-4357/aac953)
- Cranmer, S. R., Gibson, S. E., & Riley, P. 2017, *SSRv*, 212, 1345, doi: [10.1007/s11214-017-0416-y](https://doi.org/10.1007/s11214-017-0416-y)
- Cranmer, S. R., & van Ballegoijen, A. A. 2010, *ApJ*, 720, 824, doi: [10.1088/0004-637X/720/1/824](https://doi.org/10.1088/0004-637X/720/1/824)
- Cranmer, S. R., van Ballegoijen, A. A., & Edgar, R. J. 2007, *ApJS*, 171, 520, doi: [10.1086/518001](https://doi.org/10.1086/518001)
- De Pontieu, B., Erdélyi, R., & James, S. P. 2004, *Nature*, 430, 536, doi: [10.1038/nature02749](https://doi.org/10.1038/nature02749)
- Del Zanna, G., Dere, K. P., Young, P. R., & Landi, E. 2021, *ApJ*, 909, 38, doi: [10.3847/1538-4357/abd8ce](https://doi.org/10.3847/1538-4357/abd8ce)
- Dere, K. P., Landi, E., Mason, H. E., Monsignori Fossi, B. C., & Young, P. R. 1997, *A&AS*, 125, 149, doi: [10.1051/aas:1997368](https://doi.org/10.1051/aas:1997368)
- Drake, J. F., Agapitov, O., Swisdak, M., et al. 2021, *A&A*, 650, A2, doi: [10.1051/0004-6361/202039432](https://doi.org/10.1051/0004-6361/202039432)
- Dudok de Wit, T., Krasnoselskikh, V. V., Bale, S. D., et al. 2020, *ApJS*, 246, 39, doi: [10.3847/1538-4365/ab5853](https://doi.org/10.3847/1538-4365/ab5853)
- Finley, A. J., Hewitt, A. L., Matt, S. P., et al. 2019, *ApJL*, 885, L30, doi: [10.3847/2041-8213/ab4ff4](https://doi.org/10.3847/2041-8213/ab4ff4)
- Finley, A. J., Matt, S. P., Réville, V., et al. 2020, *ApJL*, 902, L4, doi: [10.3847/2041-8213/abb9a5](https://doi.org/10.3847/2041-8213/abb9a5)
- Fisk, L. A. 2003, *Journal of Geophysical Research (Space Physics)*, 108, 1157, doi: [10.1029/2002JA009284](https://doi.org/10.1029/2002JA009284)
- Fox, N. J., Velli, M. C., Bale, S. D., et al. 2016, *SSRv*, 204, 7, doi: [10.1007/s11214-015-0211-6](https://doi.org/10.1007/s11214-015-0211-6)
- Gallet, F., & Bouvier, J. 2013, *A&A*, 556, A36, doi: [10.1051/0004-6361/201321302](https://doi.org/10.1051/0004-6361/201321302)
- Geiss, J., Gloeckler, G., & von Steiger, R. 1995, *SSRv*, 72, 49, doi: [10.1007/BF00768753](https://doi.org/10.1007/BF00768753)
- Goodman, M. L., & Judge, P. G. 2012, *ApJ*, 751, 75, doi: [10.1088/0004-637X/751/1/75](https://doi.org/10.1088/0004-637X/751/1/75)
- Güdel, M. 2007, *Living Reviews in Solar Physics*, 4, 3, doi: [10.12942/lrsp-2007-3](https://doi.org/10.12942/lrsp-2007-3)
- Hamada, A., Asikainen, T., & Mursula, K. 2020, *SoPh*, 295, 2, doi: [10.1007/s11207-019-1563-y](https://doi.org/10.1007/s11207-019-1563-y)
- Hansteen, V. H., & Leer, E. 1995, *J. Geophys. Res.*, 100, 21577, doi: [10.1029/95JA02300](https://doi.org/10.1029/95JA02300)
- Harra, L. K., Sakao, T., Mandrini, C. H., et al. 2008, *ApJL*, 676, L147, doi: [10.1086/587485](https://doi.org/10.1086/587485)
- Harvey, J. W., Hill, F., Hubbard, R. P., et al. 1996, *Science*, 272, 1284, doi: [10.1126/science.272.5266.1284](https://doi.org/10.1126/science.272.5266.1284)
- Hewish, A., Scott, P. F., & Wills, D. 1964, *Nature*, 203, 1214, doi: [10.1038/2031214a0](https://doi.org/10.1038/2031214a0)
- Higginson, A. K., Antiochos, S. K., DeVore, C. R., Wyper, P. F., & Zurbuchen, T. H. 2017, *ApJ*, 837, 113, doi: [10.3847/1538-4357/837/2/113](https://doi.org/10.3847/1538-4357/837/2/113)
- Hoeksema, J. T., Wilcox, J. M., & Scherrer, P. H. 1983, *J. Geophys. Res.*, 88, 9910, doi: [10.1029/JA088iA12p09910](https://doi.org/10.1029/JA088iA12p09910)
- Horbury, T. S., Woolley, T., Laker, R., et al. 2020, *ApJS*, 246, 45, doi: [10.3847/1538-4365/ab5b15](https://doi.org/10.3847/1538-4365/ab5b15)
- Hunter, J. D. 2007, *Computing in Science and Engineering*, 9, 90, doi: [10.1109/MCSE.2007.55](https://doi.org/10.1109/MCSE.2007.55)
- Iijima, H. 2016, PhD thesis, Department of Earth and Planetary Science, School of Science, The University of Tokyo, Japan
- Irwin, J., & Bouvier, J. 2009, in *The Ages of Stars*, ed. E. E. Mamajek, D. R. Soderblom, & R. F. G. Wyse, Vol. 258, 363–374, doi: [10.1017/S1743921309032025](https://doi.org/10.1017/S1743921309032025)
- Ishikawa, R., Bueno, J. T., del Pino Alemán, T., et al. 2021, *Science Advances*, 7, eabe8406, doi: [10.1126/sciadv.abe8406](https://doi.org/10.1126/sciadv.abe8406)

- Iwai, K., Shiota, D., Tokumaru, M., et al. 2019, *Earth, Planets, and Space*, 71, 39, doi: [10.1186/s40623-019-1019-5](https://doi.org/10.1186/s40623-019-1019-5)
- . 2021, *Earth, Planets, and Space*, 73, 9, doi: [10.1186/s40623-020-01345-5](https://doi.org/10.1186/s40623-020-01345-5)
- Jackson, B. V., Hick, P. L., Kojima, M., & Yokobe, A. 1998, *J. Geophys. Res.*, 103, 12049, doi: [10.1029/97JA02528](https://doi.org/10.1029/97JA02528)
- Jacques, S. A. 1977, *ApJ*, 215, 942, doi: [10.1086/155430](https://doi.org/10.1086/155430)
- Kasper, J. C., Bale, S. D., Belcher, J. W., et al. 2019, *Nature*, 576, 228, doi: [10.1038/s41586-019-1813-z](https://doi.org/10.1038/s41586-019-1813-z)
- Kawaler, S. D. 1988, *ApJ*, 333, 236, doi: [10.1086/166740](https://doi.org/10.1086/166740)
- Keller, C. U., Schüssler, M., Vögler, A., & Zakharov, V. 2004, *ApJL*, 607, L59, doi: [10.1086/421553](https://doi.org/10.1086/421553)
- Khomenko, E., Collados, M., Díaz, A., & Vitas, N. 2014, *Physics of Plasmas*, 21, 092901, doi: [10.1063/1.4894106](https://doi.org/10.1063/1.4894106)
- Kojima, M., Tokumaru, M., Watanabe, H., et al. 1998, *J. Geophys. Res.*, 103, 1981, doi: [10.1029/97JA02162](https://doi.org/10.1029/97JA02162)
- Linker, J. A., Caplan, R. M., Downs, C., et al. 2017, *ApJ*, 848, 70, doi: [10.3847/1538-4357/aa8a70](https://doi.org/10.3847/1538-4357/aa8a70)
- Linker, J. A., Heinemann, S. G., Temmer, M., et al. 2021, arXiv e-prints, arXiv:2103.05837. <https://arxiv.org/abs/2103.05837>
- Lionello, R., Török, T., Titov, V. S., et al. 2016, *ApJL*, 831, L2, doi: [10.3847/2041-8205/831/1/L2](https://doi.org/10.3847/2041-8205/831/1/L2)
- Magyar, N., Utz, D., Erdélyi, R., & Nakariakov, V. M. 2021, *ApJ*, 914, 8, doi: [10.3847/1538-4357/abfa98](https://doi.org/10.3847/1538-4357/abfa98)
- Matt, S. P., Brun, A. S., Baraffe, I., Bouvier, J., & Chabrier, G. 2015, *ApJL*, 799, L23, doi: [10.1088/2041-8205/799/2/L23](https://doi.org/10.1088/2041-8205/799/2/L23)
- McComas, D. J., Elliott, H. A., Schwadron, N. A., et al. 2003, *Geophys. Res. Lett.*, 30, 1517, doi: [10.1029/2003GL017136](https://doi.org/10.1029/2003GL017136)
- McGregor, S. L., Hughes, W. J., Arge, C. N., & Owens, M. J. 2008, *Journal of Geophysical Research (Space Physics)*, 113, A08112, doi: [10.1029/2007JA012330](https://doi.org/10.1029/2007JA012330)
- Odstrcil, D. 2003, *Advances in Space Research*, 32, 497, doi: [10.1016/S0273-1177\(03\)00332-6](https://doi.org/10.1016/S0273-1177(03)00332-6)
- Parker, E. N. 1958, *ApJ*, 128, 664, doi: [10.1086/146579](https://doi.org/10.1086/146579)
- Pinto, R. F., & Rouillard, A. P. 2017, *ApJ*, 838, 89, doi: [10.3847/1538-4357/aa6398](https://doi.org/10.3847/1538-4357/aa6398)
- Porowski, C., Bzowski, M., & Tokumaru, M. 2021, arXiv e-prints, arXiv:2110.15847. <https://arxiv.org/abs/2110.15847>
- Reiss, M. A., MacNeice, P. J., Muglach, K., et al. 2020, *ApJ*, 891, 165, doi: [10.3847/1538-4357/ab78a0](https://doi.org/10.3847/1538-4357/ab78a0)
- Réville, V., Brun, A. S., Matt, S. P., Strugarek, A., & Pinto, R. F. 2015, *ApJ*, 798, 116, doi: [10.1088/0004-637X/798/2/116](https://doi.org/10.1088/0004-637X/798/2/116)
- Réville, V., Velli, M., Panasenco, O., et al. 2020, *ApJS*, 246, 24, doi: [10.3847/1538-4365/ab4fef](https://doi.org/10.3847/1538-4365/ab4fef)
- Riley, P., & Ben-Nun, M. 2021, *Space Weather*, 19, e02775, doi: [10.1029/2021SW002775](https://doi.org/10.1029/2021SW002775)
- Riley, P., Linker, J. A., & Arge, C. N. 2015, *Space Weather*, 13, 154, doi: [10.1002/2014SW001144](https://doi.org/10.1002/2014SW001144)
- Riley, P., Linker, J. A., & Mikić, Z. 2001, *J. Geophys. Res.*, 106, 15889, doi: [10.1029/2000JA000121](https://doi.org/10.1029/2000JA000121)
- Riley, P., Linker, J. A., Mikic, Z., et al. 2019, *ApJ*, 884, 18, doi: [10.3847/1538-4357/ab3a98](https://doi.org/10.3847/1538-4357/ab3a98)
- Riley, P., Linker, J. A., Mikić, Z., et al. 2006, *ApJ*, 653, 1510, doi: [10.1086/508565](https://doi.org/10.1086/508565)
- Sakao, T., Kano, R., Narukage, N., et al. 2007, *Science*, 318, 1585, doi: [10.1126/science.1147292](https://doi.org/10.1126/science.1147292)
- Sakurai, T. 1985, *A&A*, 152, 121
- Salpeter, E. E. 1967, *ApJ*, 147, 433, doi: [10.1086/149027](https://doi.org/10.1086/149027)
- Samara, E., Pinto, R. F., Magdalenic, J., et al. 2021, *A&A*, 648, A35, doi: [10.1051/0004-6361/202039325](https://doi.org/10.1051/0004-6361/202039325)
- Schatten, K. H. 1971, *Cosmic Electrodynamics*, 2, 232
- Schatten, K. H., Wilcox, J. M., & Ness, N. F. 1969, *SoPh*, 6, 442, doi: [10.1007/BF00146478](https://doi.org/10.1007/BF00146478)
- Schwadron, N. A., & McComas, D. J. 2021, *ApJ*, 909, 95, doi: [10.3847/1538-4357/abd4e6](https://doi.org/10.3847/1538-4357/abd4e6)
- Shiota, D., & Kataoka, R. 2016, *Space Weather*, 14, 56, doi: [10.1002/2015SW001308](https://doi.org/10.1002/2015SW001308)
- Shiota, D., Kataoka, R., Miyoshi, Y., et al. 2014, *Space Weather*, 12, 187, doi: [10.1002/2013SW000989](https://doi.org/10.1002/2013SW000989)
- Shiota, D., Tsuneta, S., Ito, H., et al. 2012, in *Astronomical Society of the Pacific Conference Series*, Vol. 454, Hinode-3: The 3rd Hinode Science Meeting, ed. T. Sekii, T. Watanabe, & T. Sakurai, 375
- Shoda, M., Chandran, B. D. G., & Cranmer, S. R. 2021, *ApJ*, 915, 52, doi: [10.3847/1538-4357/abfdbc](https://doi.org/10.3847/1538-4357/abfdbc)
- Shoda, M., Suzuki, T. K., Asgari-Targhi, M., & Yokoyama, T. 2019, *ApJL*, 880, L2, doi: [10.3847/2041-8213/ab2b45](https://doi.org/10.3847/2041-8213/ab2b45)
- Shoda, M., & Takasao, S. 2021, arXiv e-prints, arXiv:2106.08915. <https://arxiv.org/abs/2106.08915>
- Shoda, M., Yokoyama, T., & Suzuki, T. K. 2018, *ApJ*, 853, 190, doi: [10.3847/1538-4357/aaa3e1](https://doi.org/10.3847/1538-4357/aaa3e1)
- Smith, E. J., & Wolfe, J. H. 1976, *Geophys. Res. Lett.*, 3, 137, doi: [10.1029/GL003i003p00137](https://doi.org/10.1029/GL003i003p00137)
- Spitzer, L., & Härm, R. 1953, *Physical Review*, 89, 977, doi: [10.1103/PhysRev.89.977](https://doi.org/10.1103/PhysRev.89.977)
- Squire, J., Chandran, B. D. G., & Meyrand, R. 2020, *ApJL*, 891, L2, doi: [10.3847/2041-8213/ab74e1](https://doi.org/10.3847/2041-8213/ab74e1)
- Sterling, A. C., & Moore, R. L. 2020, *ApJL*, 896, L18, doi: [10.3847/2041-8213/ab96be](https://doi.org/10.3847/2041-8213/ab96be)
- Suzuki, T. K., & Inutsuka, S.-i. 2005, *ApJL*, 632, L49, doi: [10.1086/497536](https://doi.org/10.1086/497536)
- Tokumaru, M., Fujiki, K., Kojima, M., & Iwai, K. 2021, *ApJ*, 922, 73, doi: [10.3847/1538-4357/ac1862](https://doi.org/10.3847/1538-4357/ac1862)

- Tokumaru, M., Kojima, M., Fujiki, K., & Hayashi, K. 2009, *Geophys. Res. Lett.*, 36, L09101, doi: [10.1029/2009GL037461](https://doi.org/10.1029/2009GL037461)
- Tokumaru, M., Kojima, M., Fujiki, K., et al. 2011, *Radio Science*, 46, RS0F02, doi: [10.1029/2011RS004694](https://doi.org/10.1029/2011RS004694)
- Tsuneta, S., Ichimoto, K., Katsukawa, Y., et al. 2008, *ApJ*, 688, 1374, doi: [10.1086/592226](https://doi.org/10.1086/592226)
- Tsurutani, B. T., Gonzalez, W. D., Gonzalez, A. L. C., et al. 2006, *Journal of Geophysical Research (Space Physics)*, 111, A07S01, doi: [10.1029/2005JA011273](https://doi.org/10.1029/2005JA011273)
- Usmanov, A. V., Matthaeus, W. H., Goldstein, M. L., & Chhiber, R. 2018, *ApJ*, 865, 25, doi: [10.3847/1538-4357/aad687](https://doi.org/10.3847/1538-4357/aad687)
- van der Holst, B., Sokolov, I. V., Meng, X., et al. 2014, *ApJ*, 782, 81, doi: [10.1088/0004-637X/782/2/81](https://doi.org/10.1088/0004-637X/782/2/81)
- van der Walt, S., Colbert, S. C., & Varoquaux, G. 2011, *Computing in Science and Engineering*, 13, 22, doi: [10.1109/MCSE.2011.37](https://doi.org/10.1109/MCSE.2011.37)
- Velli, M. 1994, *ApJL*, 432, L55, doi: [10.1086/187510](https://doi.org/10.1086/187510)
- Verdini, A., Velli, M., Matthaeus, W. H., Oughton, S., & Dmitruk, P. 2010, *ApJL*, 708, L116, doi: [10.1088/2041-8205/708/2/L116](https://doi.org/10.1088/2041-8205/708/2/L116)
- Vidotto, A. A. 2021, *Living Reviews in Solar Physics*, 18, 3, doi: [10.1007/s41116-021-00029-w](https://doi.org/10.1007/s41116-021-00029-w)
- von Steiger, R., Schwadron, N. A., Fisk, L. A., et al. 2000, *J. Geophys. Res.*, 105, 27217, doi: [10.1029/1999JA000358](https://doi.org/10.1029/1999JA000358)
- Wang, Y. M. 2020, *ApJ*, 904, 199, doi: [10.3847/1538-4357/abbda6](https://doi.org/10.3847/1538-4357/abbda6)
- Wang, Y. M., & Sheeley, N. R., J. 1988, *J. Geophys. Res.*, 93, 11227, doi: [10.1029/JA093iA10p11227](https://doi.org/10.1029/JA093iA10p11227)
- . 1990, *ApJ*, 355, 726, doi: [10.1086/168805](https://doi.org/10.1086/168805)
- . 1995, *ApJL*, 447, L143, doi: [10.1086/309578](https://doi.org/10.1086/309578)
- Weber, E. J., & Davis, Leverett, J. 1967, *ApJ*, 148, 217, doi: [10.1086/149138](https://doi.org/10.1086/149138)
- Withbroe, G. L. 1988, *ApJ*, 325, 442, doi: [10.1086/166015](https://doi.org/10.1086/166015)
- Wold, A. M., Mays, M. L., Taktakishvili, A., et al. 2018, *Journal of Space Weather and Space Climate*, 8, A17, doi: [10.1051/swsc/2018005](https://doi.org/10.1051/swsc/2018005)
- Zank, G. P., Nakanotani, M., Zhao, L. L., Adhikari, L., & Kasper, J. 2020, *ApJ*, 903, 1, doi: [10.3847/1538-4357/abb828](https://doi.org/10.3847/1538-4357/abb828)